NANO · MICRO small
www.small-journal.com

Tailoring the Hydrophobic Interface of Core–Shell HKUST-1@Cu_2O Nanocomposites for Efficiently Selective CO_2 Electroreduction

Yan Wen, Wen-Hui Cheng, Yi-Rong Wang, Feng-Cui Shen, and Ya-Qian Lan**

The electrochemical reduction of carbon dioxide (CO_2) to ethylene creates a carbon-neutral approach to converting carbon dioxide into intermittent renewable electricity. Exploring efficient electrocatalysts with potentially high ethylene selectivity is extremely desirable, but still challenging. In this report, a laboratory-designed catalyst HKUST-1@Cu_2O/PTFE-1 is prepared, in which the high specific surface area of the composites with improved CO_2 adsorption and the abundance of active sites contribute to the increased electrocatalytic activity. Furthermore, the hydrophobic interface constructed by the hydrophobic material polytetrafluoroethylene (PTFE) effectively inhibits the occurrence of hydrogen evolution reactions, providing a significant improvement in the efficiency of CO_2 electroreduction. The distinctive structures result in the remarkable hydrocarbon fuels generation with high Faraday efficiency (FE) of 67.41%, particularly for ethylene with FE of 46.08% (−1.0 V vs RHE). The superior performance of the catalyst is verified by DFT calculation with lower Gibbs free energy of the intermediate interactions with improved proton migration and selectivity to emerge the polycarbon(C_{2+}) product. In this work, a promising and effective strategy is presented to configure MOF-based materials with tailored hydrophobic interface, high adsorption selectivity and more exposed active sites for enhancing the efficiency of the electroreduction of CO_2 to C_{2+} products with high added value.

1. Introduction

The rapid expansion of industry over the past two centuries has resulted in increasing levels of carbon dioxide in the atmosphere year after year and the accompanying environmental problems, such as global warming, which have gradually attracted the attention of the public.[1] Adopting of electricity generated from renewable energy sources such as solar and tidal power to convert carbon dioxide (CO_2) into high value-added chemical products such as methane, ethylene, and ethanol through electrochemistry techniques is a highly prospective resolution strategy.[1–3] The techniques not only reduce atmospheric carbon dioxide levels but also provide a storage option for renewable energy sources. However, the CO_2 electroreduction (CO_2RR) still faces a number of challenges due to its sluggish reaction kinetics. In addition, it has poorly controlled selectivity of the conversion of CO_2 to hydrocarbons via electrocatalysis.[4]

Copper-based catalysts are currently one kind of the most promising catalysts for the production of hydrocarbons under mild conditions in CO_2-saturated aqueous solutions.[5–7] Surface characteristics of copper and copper-based catalysts such as increasing of specific surface areas,[8] promotion of oxidation states,[9] exposure of high-index surfaces,[10,11] and engineering of surface reconstruction influence the reaction pathways.[12] However, the selectivity of controllable synthesis catalysts for reactions and the mechanism for lowering reaction energy barriers are still required to research in depth. Therefore, research of the performance and surface characterization of controllable synthesis catalysts in CO_2RR is of great significance for the reaction mechanism.

Especially, the oxidation state of copper surface affects the activity and selectivity of conversion of CO_2RR to hydrocarbon fuels.[13,14] With the ability to convert CO_2 to C_2H_4, the promising cuprous oxide(Cu_2O)-derived catalysts has been extensively investigated. As compared to conventional copper films,[15] nanocrystals,[16] or nanoparticles,[17–19] Cu_2O porous nanospheres with larger specific surface areas exhibit high conversion efficiency.[20] Generally, gas capture and adsorption in the first step are extremely important in the three-phase system for CO_2RR.[21] Thus, improving the adsorption capacity of Cu_2O porous nanospheres for CO_2 is considered to be a very promising way to further improve the overall Faraday efficiency (FE) of hydrocarbons. However, rapid performance degradation of

Y. Wen, W.-H. Cheng, F.-C. Shen
School of Biological and Chemical Engineering
Anhui Polytechnic University
Wuhu 241000, P. R. China
E-mail: fcshen@ahpu.edu.cn
Y.-R. Wang, Y.-Q. Lan
School of Chemistry
South China Normal University
Guangzhou 510006, P. R. China
E-mail: yqlan@njnu.edu.cn

The ORCID identification number(s) for the author(s) of this article can be found under https://doi.org/10.1002/smll.202307467

DOI: 10.1002/smll.202307467

single component Cu_2O during electrochemical reduction leads to the poor stability of catalytic process. Above all these factors, it is necessary to finely tailor the structure of Cu_2O so as to improve the electrochemical stability of catalysts and enable the transformation of CO_2 into hydrocarbons such as methane, ethylene, etc.[22,23] Metal-organic frameworks (MOFs) have a larger surface area, richer catalytic sites, and greater adsorption capacity for reaction intermediates owing to the porous structure, offering great potential to increase the performance of CO_2RR.[24] It makes sense that a combination of Cu_2O and Cu-based MOFs can be used to improve the catalytic performance by exploiting the synergistic effect.

Promisingly, core–shell structure catalysts displayed the enormous potential to be used in electrochemical CO_2RR owing to the interface effect and tandem catalysis.[25] In particular, the core–shell structured copper-based catalysts with enhanced C—C coupling on catalysts surface can be facilitated by the strong synergistic interaction between cores and shells, which modulates the electronic configuration of environment on the catalyst surface and the adsorption of intermediates in an electrochemical process.[26] Consequently, it is possible to dramatically increase the electrochemical properties of CO_2RR with core–shell Cu-based catalysts while guaranteeing a high FE for the C_{2+} product. Furthermore, the outer shell portion of the core–shell structure acts as a physical shield to keep the active sites inside from loss and accumulation.[27] Hydrophilicity has a non-negligible effect on the performance of CO_2RR, since electrolyte infiltrates pores of gas diffusion layer (GDL), decreases of hydrophobicity leading to an increase in diffusion distance of CO_2 and preventing the transport of CO_2 to catalyst sites,[28] while hydrophilic conditions favor the occurrence of side reactions (HER), resulting in the poor efficiency of electroreduction of CO_2 to C_{2+} products.[29,30] In addition, the overflow affects the selectivity of CO_2RR as restricting the transport of CO_2 to the active sites promotes hydrogen evolution reaction (HER).[31] To further inhibit the competing reaction for HER, tailoring the hydrophobic interface is used to block the supply of protons to Cu_2O nanosphere electrode while allowing CO_2 to enter the electrode, which would be a prospective method of enhancing CO_2RR and inhibiting HER.[32]

Following the high adsorptive property of HKUST-1 for CO_2 to promote the continuous three-phase reaction and improved coupling of CO* and *CHO by Cu_2O,[33] the dimerization of CO* will be facilitated by HKUST-1@Cu_2O, thus improving the selectivity of the catalyst for C_{2+} products. Besides, modulating the hydrophobicity of material (PTFE) improves selectivity and also prevents side reactions from occurring. Benefiting from the ingenious construction of the system, the HKUST-1@Cu_2O/PTFE-1 catalyst exhibits a current density of −70.13 mA cm^{-2} at −1.0 V and a selectivity of 67.41% for hydrocarbon fuels generation.

2. Results and Discussion

A scheme for the preparation of catalysts for CO_2RR by a simple method is illustrated in **Figure 1**. First, $Cu(NO_3)_2{\cdot}3H_2O$ and the prepared HKUST-1 were added and stirred continuously. Then, an appropriate amount of ascorbic acid solution was added and the color of the solution changed from blue to orange. The products in solution were obtained by centrifugation and washed twice with distilled water and ethanol, respectively. Subsequently,

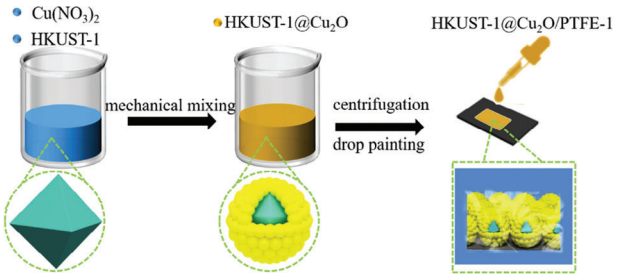

Figure 1. Schematic illustration of the synthetic process of HKUST-1@Cu_2O/PTFE-1 composite.

HKUST-1@Cu_2O was obtained after drying in an oven at 60 °C overnight. Finally, 5 mg sample was dispersed in a mixture of distilled water, ethanol, and PTFE by an ultrasound treatment for 30 min. As-prepared catalyst ink (50 µL) was sprayed directly onto hydrophobic carbon paper to form an area of 0.5 × 1 cm^2, which was further dried at room temperature.

The X-ray diffraction (XRD) patterns of HKUST-1@Cu_2O/PTFE-1, HKUST-1@Cu_2O, HKUST-1, and Cu_2O samples are shown in **Figure 2**a. The XRD pattern of HKUST-1@Cu_2O displayed the main diffraction peaks (29.55°, 36.42°, 42.30°, 61.35° 73.53°, and 77.32°) of crystalline Cu_2O (JCPDS No.1-1142) and characteristic peaks (6.66°, 10.42°, 11.55°, 13.43°, and 18.93°) of HKUST-1 (simulation), indicating that the catalyst was successfully synthesized. After decoration of PTFE, the catalyst showed its characteristic peak at 18.0° without structural changes. Scanning electron microscopy (SEM) was adopted to explore the surface morphology of HKUST-1@Cu_2O (Figure 2b), HKUST-1@Cu_2O/PTFE-1 (Figure 2c), and HKUST-1 (Figure S1, Supporting Information) as prepared. Figure 2b illustrated the presence of pores on the surface of nanospheres. An average diameter of 300 nm was observed for the highly uniform spherical nanoparticles, and the rough porous surface morphology of HKUST-1@Cu_2O facilitated its adsorption of CO_2. The hydrophobic layer interface on the surface of core–shell structure was clearly shown in Figure 2c. The high-resolution transmission electron microscope (HRTEM) in Figure 2d revealed that the lattice spacing of 0.245 nm corresponds to 111 crystal plane of Cu_2O (JCPDS No. 1–1142) and the interface of HKUST-1 and Cu_2O.[34] According to the transmission electron microscopy (TEM) (Figure 2e) image, the core–shell structure of HKUST-1@Cu_2O was observed, which will be conducive to improving the ability of catalysts to capture the CO_2. In addition, the elemental mapping images revealed that Cu and O were uniformly distributed on the HKUST-1@Cu_2O sample, as shown in Figure 2f–i. These features are conducive to the increase of active site and improving the catalytic performance. All the above characterizations demonstrate that the core–shell nanosphere structure consisting of HKUST-1 and Cu_2O was fabricated. The composition of HKUST-1@Cu_2O was further analyzed by Fourier Transform Infrared Spectroscopy (FTIR). As shown in Figure S2 (Supporting Information), a peak at 492 cm^{-1} was associated with the bond of Cu and O in ligand of BTC,[35] and the peak at 630 cm^{-1} appeared to originate from stretching vibrations of Cu(I)-O in Cu_2O.[36] Furthermore, the peaks positioned at 1625 and 1375 cm^{-1} corresponded to —COO— and C—C asymmetric stretching in the phenyl ring, respectively.[37]

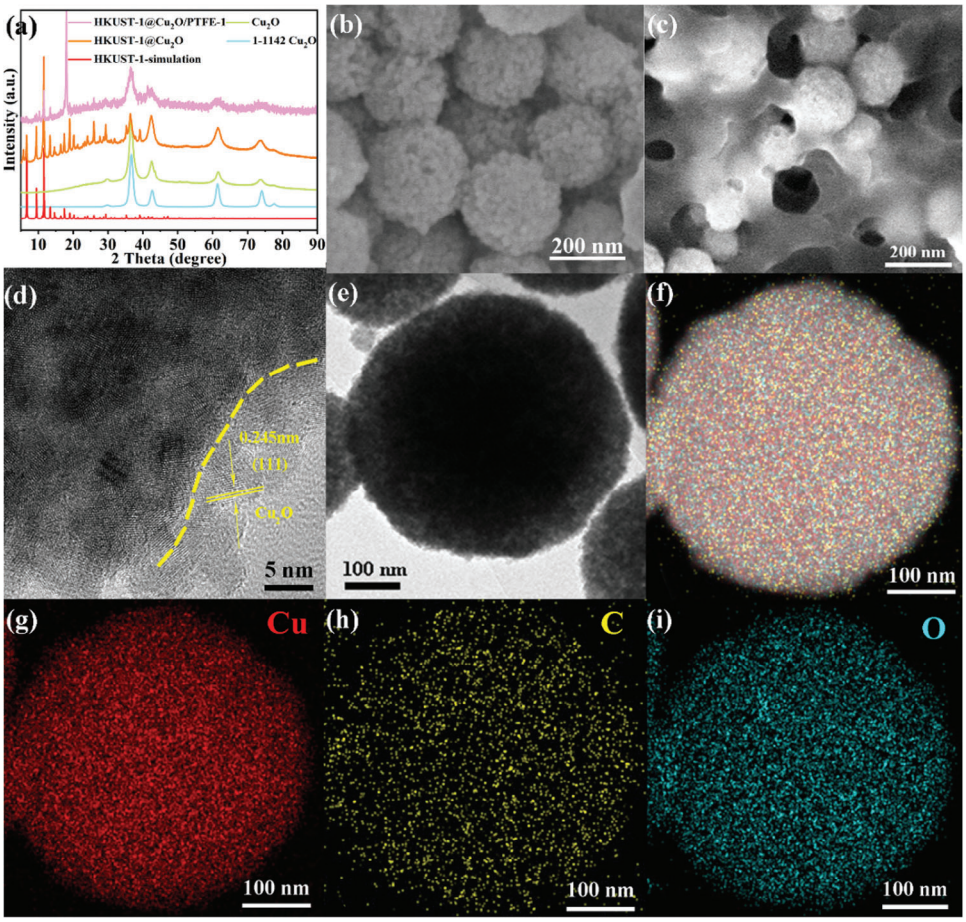

Figure 2. Electrochemical properties of catalysts. a) XRD patterns of the HKUST-1@Cu_2O relative composites, b) SEM images of HKUST-1@Cu_2O nanospheres, c) SEM images of HKUST-1@Cu_2O/PTFE-1, d) HRTEM images of HKUST-1@Cu_2O, e–i) TEM and the corresponding EDX elemental mapping images of HKUST-1@Cu_2O.

The presence of Cu C and O elements on the electrochemical catalysts was confirmed by energy dispersive X-ray spectroscopy (EDS, Figure S3, Supporting Information) matching with the mapping elements distribution. Moreover, a comparison of BET surface areas of Cu_2O and HKUST-1@Cu_2O was presented in Table S1 (Supporting Information). The specific surface area of HKUST-1@Cu_2O was almost 5 times higher than that of Cu_2O, indicating that loading HKUST-1 increased the gas adsorption and specific surface area of active material for the three-phase reaction for CO_2RR. The nitrogen(N_2) adsorption and desorption curves showed that the adsorption of HKUST-1@Cu_2O toward N_2 was higher than that of Cu_2O (Figure S4a, Supporting Information), suggesting that the superior adsorption properties of HKUST-1@Cu_2O. To estimate the CO_2 adsorption ability of HKUST-1@Cu_2O, the CO_2 adsorption testing was performed. The CO_2 uptake capacities of HKUST-1@Cu_2O and Cu_2O at 273 K were 77.1976 and 59.6527 $cm^3\ g^{-1}$, respectively (Figure S4b, Supporting Information). The excellent adsorption properties of CO_2 by the catalyst may be one of the potential factors enabling the enhanced catalytic performance.

The elemental composition and chemical state of HKUST-1@Cu_2O were investigated via X-ray photoelectron spectroscopy (XPS) with major elements of Cu, O, and C (Figure S5a, Supporting Information). The C 1s spectrum (Figure S5b, Supporting Information) showed two binding energies at 284.6 and 288 eV, corresponding to the C═C and O—C═O groups in organic linkers.[38] Cu(I) 2p3/2 and Cu(I) 2p1/2 with binding energies of 931.8 and 951.6 eV, respectively, were consistent with Cu (I) (Figure S5c, Supporting Information).[39] Furthermore, the 934.2 and 954.1 eV satellite peaks as well as the two 942.3 and 954.2 eV peaks were corresponded to Cu(II) 2p3/2 and Cu(II) 2p1/2, suggesting the existence of Cu^{2+} in HKUST-1.[40] The XPS spectrum of O 1s (Figure S5d, Supporting Information) displayed two peaks at 530 and 530.6 eV, corresponding to metal-oxygen and adsorbed—OH, respectively.[41] These results confirmed the valence states of copper ions on the surface of catalysts.

To evaluate the electrochemical CO_2RR performance of the catalysts in a flow cell with diverse potentials, the CO_2RR capability of composite HKUST-1@Cu_2O/PTFE-1 was investigated and compared with Cu_2O and HKUST-1. The linear sweep voltammetry(LSV) curves in **Figure 3**a demonstrated that HKUST-1@Cu_2O/PTFE-1 offered a higher current density in CO_2—saturated electrolyte than in Ar-saturated electrolyte conditions, contributing to an effective increase in CO_2RR efficiency. To assess the catalyst selectivity for CO_2RR, the gas/liquid phase reduction products were analyzed by gas chromatography and

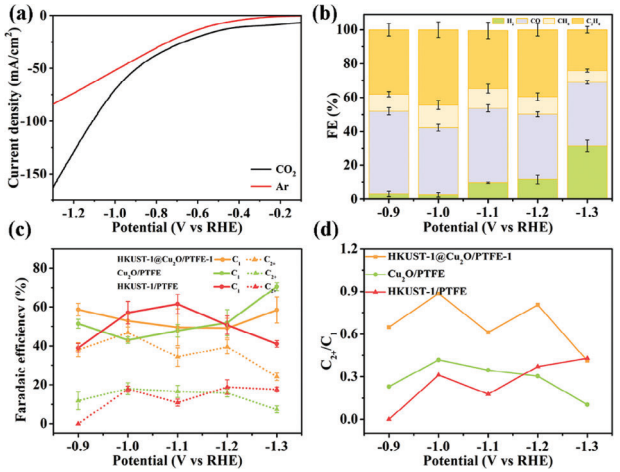

Figure 3. Electrochemical properties of catalysts in a flow cell. a) LSV curves at a scan rate of 50 mV s^{-1} in Ar and CO_2-saturated electrolyte, respectively, b) the product distribution for CO_2RR at different potentials, c) C_{2+} and C_1 Faradaic efficiencies, and d) C_{2+}/C_1 product selectivity on catalysts at different applied potentials.

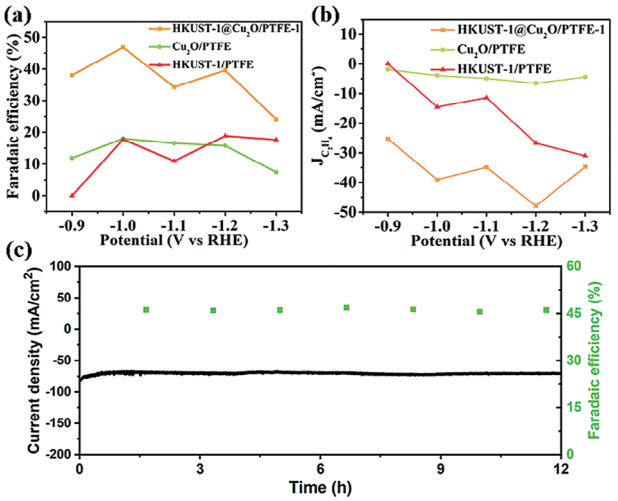

Figure 4. Electrochemical properties of catalysts. a) Faradaic efficiencies for C_2H_4 on the three types of catalysts at different applied potentials, b) C_2H_4 partial current densities obtained on catalysts at different applied potentials, c) Faradaic efficiency for C_2H_4 in stability test at −1.0 V versus RHE.

nuclear magnetic resonance hydrogen spectrum, respectively. As a result, CO, CH_4, and C_2H_4 were detected as the majority products with high Faraday efficiency(FE) and there were no liquid products (Figure S6, Supporting Information). Interestingly, the maximum FE_{C2H4} (46.08%) as well as 26.72% FE_{CO} and 21.33% FE_{CH4} and negligible FE_{H2} (5.15%) was achieved at −1.0 V for HKUST-1@Cu_2O/PTFE-1(Figure 3b). The CO_2RR electrolysis revealed that the selectivity for C_{2+} products of HKUST-1@Cu_2O/PTFE-1 was significantly superior to that of HKUST-1@Cu_2O and Cu_2O/PTFE in the range of −0.9–−1.3 V versus RHE (Figure 3c). The significant degree of selectivity for the C_{2+} compound of HKUST-1@Cu_2O/PTFE-1 was also illustrated in Figure 3d at each of the potentials. Especially, the C_{2+}/C_1 ratio of the catalyst reaches ≈0.9 at the potential of −1.0 V versus RHE, demonstrating considerably superior performance than other controlled catalysts.

A comparison of the FE of composite HKUST-1@Cu_2O/PTFE-1 with that of Cu_2O/PTFE and HKUST-1/PTFE for the generation of C_2H_4 at various potentials was illustrated in **Figure 4**a. Cu_2O/PTFE and HKUST-1/PTFE obtained the low FE of C_2H_4 with 17.98% (Figure S7a, Supporting Information) and 10.63% (Figure S7b, Supporting Information) at −1.0 V versus RHE, respectively. By contrast, HKUST-1@Cu_2O/PTFE-1 achieved higher FE for C_2H_4 products, especially with the greatest FE of 46.08%, even higher than many Cu-based catalysts reported in literatures (Figure S8, Supporting Information). The partial current densities of C_2H_4 at different potentials were calculated in Figure 4b to further reveal the catalytic activity of HKUST-1@Cu_2O/PTFE-1. Significantly, the HKUST-1@Cu_2O/PTFE-1 catalyst exhibits the highest selectivity for C_2H_4 when the voltage is −1.0 V versus RHE, which is consistent with the trend in Figure 4a. The high partial current density for C_2H_4 significantly illustrated that encapsulation of HKUST-1 in Cu_2O enhanced the ability of adsorbing CO_2 gas and hydrophobic property of PTFE decoration on the surface inhibited the generation of H_2, improving the performance of the catalyst.

To elucidate the impact of core MOFs on the electroreduction performance of catalysts, the composite ZIF-8@Cu_2O was successfully synthesized as Figure S9 (Supporting Information). The corresponding catalytic activity of ZIF-8@Cu_2O/PTFE was also assessed for comparison as Figure S10a,b (Supporting Information). Most notably, it obtained FE of 24.07% for C_2H_4 and a C_1/C_{2+} ratio of 2.91 at −1.0 V versus RHE, the overall performance was superior to that of Cu_2O/PTFE and inferior to that of HKUST-1@Cu_2O/PTFE-1. Obviously, it can be inferred that the core of MOFs was conducive to the adsorption of CO_2 on the catalyst surface. In addition, HKUST-1 and Cu_2O, as the active sites, were more likely to interact with key reaction intermediates and promote the dimerization with the aid of strong adsorption of carbon dioxide by MOFs. Thus, the synergistic effect of core and shell components maximized its catalytic activity. Based on the improved performance after the core of HKUST-1 compounding, the effect of HKUST-1 with different loadings on the catalyst of CO_2RR efficiency was also explored and labeled as HKUST-1@Cu_2O/PTFE-2 and 3, respectively. When the mass of HKUST-1 of catalysts was reduced, the reduction products obtained are mainly H_2, CO, and CH_4(Figure S10c, Supporting Information), which may be due to the reduced amount of CO_2 adsorption with short residence time, it is not conducive to the intermediate dimerization reaction in catalysts, affecting the generation of C_{2+} products (Figure S11, Supporting Information). However, the addition of excess HKUST-1 will reduce the electrons transfer rate of the catalyst for its poor electrical conductivity, resulting in the poor catalytic performance and generation efficiency of reduction products (Figures S10d and S11, Supporting Information).

During the electrolysis process, the equilibrium between gas and liquid in a GDE (flow cell with gas diffusion electrodes) may be disrupted as the electrodes become hydrophilic owing to electrochemical refinement and consequently the pores of the catalyst layer are submerged with electrolyte, which inhibits mass transfer and leads to a decrease in the rate of reaction.[42] Considering the inhibitory effect of hydrophobicity on HER, PTFE

was adopted to form a hydrophobic surface on the catalyst surface in the electrode preparation process for a balanced gas/liquid environment during the electrolysis process, creating a durable solid-liquid-gas interface benefiting for the electrolysis of CO_2 (Figures S12 and S13, Supporting Information). The inhibition of HER and the effect on the catalytic performance of different amounts of PTFE were investigated during the preparation of the electrodes, marked as HKUST-1@Cu_2O/PTFE-4, 5, and 6, respectively. High selectivity of the catalyst for H_2 was observed without PTFE and 10 uL PTFE added. However, the excess wettability modification made poor contact between the catalyst and electrolyte, thus decreasing the catalytic performance. The contact angle between the droplet and catalyst was further characterized to illustrate the effect of different amounts of PTFE on the hydrophobicity of the catalyst surface. The contact angles of HKUST-1@Cu_2O/PTFE-1 were 124° and 117°, respectively, before and after electrolysis (Figure S14a,b, Supporting Information). It was shown that the catalysts maintained hydrophobicity after PTFE decoration protecting the catalysts layer from flooding, which permitted the catalysts layer to sustain a balanced gas/liquid microenvironment and created a persistent solid-liquid-gas interface for CO_2 electrolysis. It is important to note that an insufficient or an excess amount of PTFE (Figure S14c,d, Supporting Information) will negatively affect the performance of catalysts for the insufficient wettability modification will facilitate HER, and too excessive wettability modification will affect the performance by interfering with the three-phase reaction.

Electrochemical impedance spectroscopy was carried out on the samples in order to investigate the electrocatalytic kinetics of the electrode/electrolyte surface during CO_2RR (Figure S15, Supporting Information). As evidenced by the Nyquist plots and Table S2 (Supporting Information), the resistance value of HKUST-1@Cu_2O/PTFE-1 (387.373 Ω) with the favorable reaction kinetics was lower than that of Cu_2O (748.885 Ω) and HKUST-1 (1284.482 Ω). HKUST-1 had a high resistance, but the resistance value was successfully reduced by compounding with Cu_2O. Moreover, the addition of excess PTFE material increased the resistance of catalysts and reduced the charge transfer efficiency. Stability is an essential standard for evaluating the sustainability of catalysts. For the purpose of analyzing the electrochemical resistance of HKUST-1@Cu_2O/PTFE-1, long-term durability tests were evaluated by chronoamperometric curves at −1.0 V versus RHE (Figure 4c). It can be expected that the catalyst manifested negligible current decay and excellent stability within 12 h. Correspondingly, we noticed that the FE_{C2H4} of the catalyst remained ≈46.08% without any obvious decrease. After the stability experiments, the samples were analyzed by XRD and IR (Figure S16, Supporting Information). Obviously, the characteristic peaks of Cu_2O (29.55°, 36.42°, 42.30°, 61.35° 73.53°, and 77.32°) and HKUST-1 (6.66°, 10.42°, 11.55°, 13.43°, and 18.93°) as well as the characteristic peaks of IR spectra were practically unchanged, demonstrating the remarkable stability of HKUST-1@Cu_2O/PTFE-1 catalysts.

First-principle calculations were carried out using density functional theory (DFT) with generalized gradient approximation (GGA) of Perdew–Burke–Ernzerhof (PBE) implemented in the Vienna Ab-Initio Simulation Package (VASP).[43,44] The valence electronic states were expanded on the basis of plane waves with the core-valence interaction represented using the projector augmented plane wave (PAW) approach[45] and a cutoff of 520 eV. A Γ-centered *k*-mesh of 1 × 1 × 1 was employed for the surface calculations. Convergence was achieved when the forces acting on ions become smaller than 0.02 eV $Å^{-1}$. Based on the normal mechanism of *CHO—*CHO coupling, DFT calculations were utilized to elucidate the pathway for the conversion of CO_2 to C_2H_4 by Cu_2O and HKUST-1@Cu_2O catalysts in CO_2RR (Figures S17 and S18, Supporting Information). For the HKUST-1@Cu_2O catalyst, molecules of CO_2 were hydronated to create *COOH intermediates with C atoms connecting to Cu sites, and then reduced to H_2O and *CO intermediates, which further absorbed H atoms to produce the first *CHO intermediates with endothermic properties. The CO_2 molecules near the catalyst were attracted to the resulting *CHO intermediate for the second hydrogenation step, forming the *CHO+*COOH intermediates, and subjected to two-step hydrogenation to produce the *CHO+*CHO intermediates. Ultimately, *CHO+*CHO proceeded through self-coupling and hydrogenation resulting in the formation of C_2H_4. The variation of absorbed Gibbs free energy per intermediate during CO_2RR for Cu_2O and HKUST-1@Cu_2O catalysts was described in **Figure 5**a. The hydrogenation of gaseous CO_2 molecules absorbed on the surface of HKUST-1@Cu_2O needs a Gibbs free energy of −0.68 eV, which was lower than that of Cu_2O (−0.37 eV) proving that CO_2 molecules were more likely to occur on the surface of HKUST-1@Cu_2O/PTFE-1 in terms of activation. Notably, the required free energy for the decomposition of *COOH into H_2O molecules and *CO on HKUST-1@Cu_2O is the minimum, demonstrating that HKUST-1@Cu_2O is remarkably favorable for the generation of *CO. Meanwhile, the *CO hydrogenation to *CHO and *CHO coupling to *OHC—CHO in the CO_2RR pathway are two critical processes to initiate C_2H_4 production. The conversion of *CHO to *OHC—CHO has three kinds of intermediate structures with increased practical energy needed for this reaction. In particular, HKUST-1@Cu_2O shows the least Gibbs free energy required to generate these three intermediate structures, and the Gibbs free energies for the generation of *OHC—CHO intermediates on HKUST-1@Cu_2O and Cu_2O are −0.41 and −0.27 eV, respectively. Therefore, the interaction path from *CO to *CHO and then to *OHC—CHO is extremely advantageous for the formation of C_2H_4 products at the surface of HKUST-1@Cu_2O, contributing to the high selectivity of the catalyst for C_2H_4. Comparatively, HKUST-1@Cu_2O has a stronger binding strength with reaction intermediate compared to pure Cu_2O owing to the following reason: HKUST-1 as the metal-organic framework (MOF) contains coordinatively unsaturated metal sites, which can increase the electron density. As shown in the differential charge density distribution (Figure 5b), the interaction between Cu_2O and HKUST-1 enhances the electron density of Cu_2O, benefiting for the two key reactions of hydrogenation of *CO to form *CHO and the coupling of *CHO to *OHC—CHO intermediate for C_2H_4 in CO_2RR.

3. Conclusion

Here, we have synthesized highly efficient catalysts for the CO_2RR by encapsulating HKUST-1 in Cu_2O nanospheres and incorporating the hydrophobic material PTFE on the electrodes

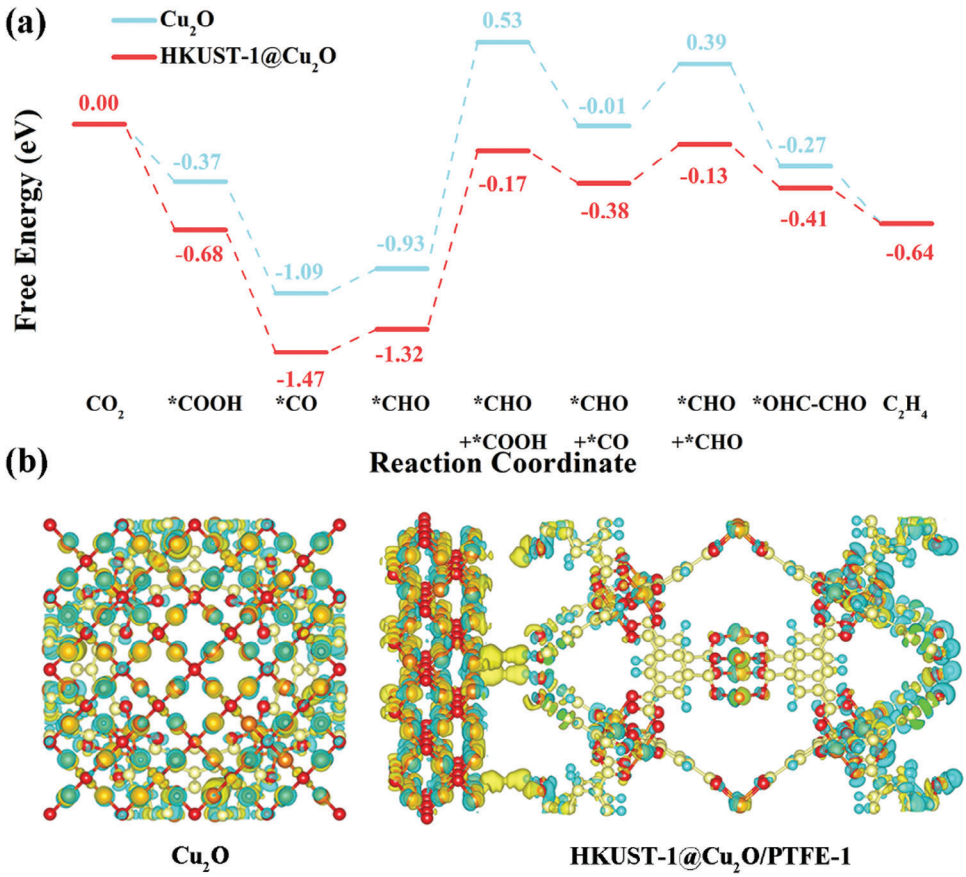

Figure 5. Mechanistic investigation of Cu_2O and HKUST-1@Cu_2O. a) DFT-calculated Gibbs free energy of the Cu_2O and HKUST-1@Cu_2O catalysts, b) differential charge density distribution of Cu_2O and HKUST-1@Cu_2O.

surface. Especially, the composite HKUST-1@Cu_2O/PTFE-1 shows a high FE of 67.41% for the composition of hydrocarbon fuel products, notably for C_2H_4 (46.08%), benefiting from the ingenious design of the catalysts, in which Cu_2O and HKUST-1 act as the active sites, the high adsorption of CO_2 for HKUST-1 provides the possibility of dimerization and C_{2+} product generation, and the hydrophobicity interface of PTFE effectively inhibiting the HER process. The enhanced performance of the catalyst may be ascribed to the lower Gibbs free energy of the intermediate interactions generating the C_2H_4 product, which is considerably advantageous for proton migration and the improvement of selectivity, as demonstrated by the experimental results and DFT calculations. This report shed insight on the activity and selectivity of elaborately designed electrocatalysts from the hydrophobic surface adsorption-desorption properties of MOF-based materials for modulating the catalysts of CO_2RR.

4. Experimental Section

Chemicals, materials, and the preparation of catalysts are shown in Supporting Information.

Supporting Information

Supporting Information is available from the Wiley Online Library or from the author.

Acknowledgements

Y.W. and W.H.C. contributed equally to this work. This work was financially supported by the National Natural Science Foundation of China (no. 21901003), and the Anhui Provincial Department of Education (no. KJ2019A0139).

Conflict of Interest

The authors declare no conflict of interest.

Data Availability Statement

The data that support the findings of this study are available from the corresponding author upon reasonable request.

Keywords

CO_2 electroreduction, Cu_2O, core–shell, hydrophobic interface, metal-organic frameworks (MOFs)

Received: August 27, 2023
Revised: October 18, 2023
Published online:

[1] H. Zhang, X. Chang, J. G. Chen, W. A. Goddard, B. Xu, M.-J. Cheng, Q. Lu, *Nat. Comm.* **2019**, *10*, 3340.
[2] S. Popovic, M. Smiljanic, P. Jovanovic, J. Vavra, R. Buonsanti, N. Hodnik, *Angew. Chem., Int. Ed.* **2020**, *59*, 14736.
[3] X. Chen, J. Chen, N. M. Alghoraibi, D. A. Henckel, R. Zhang, U. O. Nwabara, K. E. Madsen, P. J. A. Kenis, S. C. Zimmerman, A. A. Gewirth, *Nat. Catal.* **2021**, *4*, 20.
[4] F.-Y. Gao, S.-J. Hu, X.-L. Zhang, Y.-R. Zheng, H.-J. Wang, Z.-Z. Niu, P.-P. Yang, R.-C. Bao, T. Ma, Z. Dang, Y. Guan, X.-S. Zheng, X. Zheng, J.-F. Zhu, M.-R. Gao, S.-H. Yu, *Angew. Chem., Int. Ed.* **2020**, *59*, 8706.
[5] J. Li, H. Huang, W. Xue, K. Sun, X. Song, C. Wu, L. Nie, Y. Li, C. Liu, Y. Pan, H.-L. Jiang, D. Mei, C. Zhong, *Nat. Catal.* **2021**, *4*, 719.
[6] G. Singh, J. Lee, A. Karakoti, R. Bahadur, J. Yi, D. Zhao, K. Albahily, A. Vinu, *Chem. Soc. Rev.* **2020**, *49*, 4360.
[7] Y. Wang, Z. Wang, C.-T. Dinh, J. Li, A. Ozden, M. Golam Kibria, A. Seifitokaldani, C.-S. Tan, C. M. Gabardo, M. Luo, H. Zhou, F. Li, Y. Lum, C. Mccallum, Y. Xu, M. Liu, A. Proppe, A. Johnston, P. Todorovic, T.-T. Zhuang, D. Sinton, S. O. Kelley, E. H. Sargent, *Nat. Catal.* **2020**, *3*, 98.
[8] M. Hu, L. Jin, Y. Zhu, L. Zhang, X. Lu, P. Kerns, X. Su, S. Cao, P. Gao, S. L. Suib, B. Liu, J. He, *Appl Catal B* **2020**, *264*, 118553.
[9] K. M. Cho, W.-B. Jung, D. Kim, J. Y. Kim, Y. Kim, G.-T. Yun, S. Ryu, A. Al-Saggaf, I. Gereige, H.-T. Jung, *J. Mater. Chem. A* **2020**, *8*, 14592.
[10] J.-D. Yi, R. Xie, Z.-L. Xie, G.-L. Chai, T.-F. Liu, R.-P. Chen, Y.-B. Huang, R. Cao, *Angew. Chem., Int. Ed.* **2020**, *59*, 23641.
[11] C. Zhao, X. Su, S. Wang, Y. Tian, L. Yan, Z. Su, *J. Mater. Chem. A* **2022**, *10*, 6178.
[12] X.-L. Shi, B. Sun, Q. Hu, K. Liu, P. Li, B. Liu, *Chem. Eng. J.* **2020**, *395*, 125084.
[13] H. Mistry, A. S. Varela, C. S. Bonifacio, I. Zegkinoglou, I. Sinev, Y.-W. Choi, K. Kisslinger, E. A. Stach, J. C. Yang, P. Strasser, B. R. Cuenya, *Nat. Comm.* **2016**, *7*, 12945.
[14] W.-M. Wang, W.-T. Wang, M.-Y. Wang, A.-L. Gu, T.-D. Hu, Y.-X. Zhang, Z.-L. Wu, *Inorg. Chem.* **2021**, *60*, 9122.
[15] K. Liu, M. Ma, L. Wu, M. Valenti, D. Cardenas-Morcoso, J. P. Hofmann, J. Bisquert, S. Gimenez, W. A. Smith, *ACS Appl. Mater. Interfaces* **2019**, *11*, 16546.
[16] Z. Zhang, R. You, W. Huang, *Chinese.J. Chem.* **2022**, *40*, 846.
[17] C. Kim, K. M. Cho, K. Park, J. Y. Kim, G.-T. Yun, F. M. Toma, I. Gereige, H.-T. Jung, *Adv. Funct. Mater.* **2021**, *31*, 2102142.
[18] S. Wang, T. Kou, J. B. Varley, S. A. Akhade, S. E. Weitzner, S. E. Baker, E. B. Duoss, Y. Li, *ACS Mater. Lett.* **2021**, *3*, 100.
[19] L. Xiong, X. Zhang, L. Chen, Z. Deng, S. Han, Y. Chen, J. Zhong, H. Sun, Y. Lian, B. Yang, X. Yuan, H. Yu, Y. Liu, X. Yang, J. Guo, M. H. Rümmeli, Y. Jiao, Y. Peng, *Adv. Mater.* **2021**, *33*, 2101741.
[20] P.-P. Yang, X.-L. Zhang, F.-Y. Gao, Y.-R. Zheng, Z.-Z. Niu, X. Yu, R. Liu, Z.-Z. Wu, S. Qin, L.-P. Chi, Y. Duan, T. Ma, X.-S. Zheng, J.-F. Zhu, H.-J. Wang, M.-R. Gao, S.-H. Yu, *J. Am. Chem. Soc.* **2020**, *142*, 6400.
[21] P. An, L. Wei, H. Li, B. Yang, K. Liu, J. Fu, H. Li, H. Liu, J. Hu, Y.-R. Lu, H. Pan, T.-S. Chan, N. Zhang, M. Liu, *J. Mater. Chem. A* **2020**, *8*, 15936.
[22] X. Chang, A. Malkani, X. Yang, B. Xu, *J. Am. Chem. Soc.* **2020**, *142*, 2975.
[23] W. B. Huang, F. Y. Ren, M. W. Wang, L. Q. Qiu, K. H. Chen, L. N. He, **2020**, *85*, 14109.
[24] T. Yan, P. Wang, W.-Y. Sun, *Small* **2023**, *19*, 2206070.
[25] S. Nitopi, E. Bertheussen, S. B. Scott, X. Liu, A. K. Engstfeld, S. Horch, B. Seger, I. E. L. Stephens, K. Chan, C. Hahn, J. K. Nørskov, T. F. Jaramillo, I. Chorkendorff, *Chem. Rev.* **2019**, *119*, 7610.
[26] M. Jouny, G. S. Hutchings, F. Jiao, *Nat. Catal.* **2019**, *2*, 1062.
[27] A. Vasileff, C. Xu, Y. Jiao, Y. Zheng, S.-Z. Qiao, *Chem* **2018**, *4*, 1809.
[28] R. Du, Q. Wu, S. Zhang, P. Wang, Z. Li, Y. Qiu, K. Yan, G. I. N. Waterhouse, P. Wang, J. Li, Y. Zhao, W.-W. Zhao, X. Wang, G. Chen, *Small* **2023**, *19*, 2301289.
[29] Y. Wu, L. Charlesworth, I. Maglaya, M. N. Idros, M. Li, T. Burdyny, G. Wang, T. E. Rufford, *ACS Energy Lett.* **2022**, *7*, 2884.
[30] K. Yang, R. Kas, W. A. Smith, T. Burdyny, *ACS Energy Lett.* **2021**, *6*, 33.
[31] T. N. Nguyen, C.-T. Dinh, *Chem. Soc. Rev.* **2020**, *49*, 7488.
[32] Y. Huang, P. Du, W.-X. Shi, Y. Wang, S. Yao, Z.-M. Zhang, T.-B. Lu, X. Lu, *Appl Catal B* **2021**, *288*, 120001.
[33] Y. Wang, J. Liu, G. Zheng, *Adv. Mater.* **2021**, *33*, 2005798.
[34] X. Tan, C. Yu, C. Zhao, H. Huang, X. Yao, X. Han, W. Guo, S. Cui, H. Huang, J. Qiu, *ACS Appl. Mater. Interfaces* **2019**, *11*, 9904.
[35] M. S. Alhumaimess, A. A. Essawy, M. M. Kamel, I. H. Alsohaimi, H. M. A. Hassan, *Nanomaterials* **2020**, *10*, 781.
[36] M. R. Azhar, H. R. Abid, H. Sun, V. Periasamy, M. O. Tadé, S. Wang, *J. Colloid Interf. Sci.* **2016**, *478*, 344.
[37] M. R. Azhar, G. Hussain, M. O. Tade, D. S. Silvester, S. Wang, *ACS Appl. Nano Mater.* **2020**, *3*, 4376.
[38] Y. Wu, X. Li, H. Zhao, F. Yao, J. Cao, Z. Chen, D. Wang, Q. Yang, *Chem. Eng. J.* **2021**, *426*, 131255.
[39] H. Cheng, M.-L. Li, C.-Y. Su, N. Li, Z.-Q. Liu, *Adv. Funct. Mater.* **2017**, *27*, 1701833.
[40] L. Yu, G. Li, X. Zhang, X. Ba, G. Shi, Y. Li, P. K. Wong, J. C. Yu, Y. Yu, *ACS Catal.* **2016**, *6*, 6444.
[41] L. An, L. Huang, P. Zhou, J. Yin, H. Liu, P. Xi, *Adv. Funct. Mater.* **2015**, *25*, 6814.
[42] Z. Xing, L. Hu, D. S. Ripatti, X. Hu, X. Feng, *Nat. Comm.* **2021**, *12*, 136.
[43] G. Kresse, J. Furthmüller, *Phy. Rev.* **1996**, *54*, 11169.
[44] J. P. Perdew, K. Burke, M. Ernzerhof, *Phy. Rev. Lett.* **1996**, *77*, 3865.
[45] P. E. Blöchl, *Phy. Rev.* **1994**, *50*, 17953.